Exact Beltramian Solution of the Bidirectional Vortex Motion in a Capped Ellipsoidal Cyclonic Rocket Engine

Patrick Eid* and Joseph Majdalani†
Auburn University, Auburn, AL 36849

This work develops an inviscid Beltramian solution for the cyclonic motion engendered in a bidirectional vortex engine with a semi-ellipsoidal chamber configuration. The swirling motion is initiated by a tangentially injected gaseous stream at the inner circumference of the chamber's equatorial plane. The ensuing helical updraft adheres to the chamber dome, reverses direction while curving around, and exits through the central core. The present analysis is based on the Bragg-Hawthorne equation, a compact streamfunction formulation that is well adapted to model steady, incompressible, and axisymmetric helical motions. By enforcing appropriate boundary conditions, an analytical solution is obtained for the Stokes streamfunction in oblate spheroidal coordinates. Being a parent function, the streamfunction enables us to derive expressions for fundamental flow properties assuming both prolate and oblate ellipsoidal configurations. Owing to the intrinsic ellipsoidal curvature, the cyclonic stream also gives rise to a polar mantle across which the flow transitions to a purely radial inward motion. Along this lower ellipsoidal boundary, the polar velocity vanishes once while reversing its angular orientation. Both the polar and axial mantles merge in the exit plane, where the ideal outlet radius of the chamber can be deduced from this collocated position. The latter leads to an optimal exit diameter of approximately 61.06 percent of the capped-ellipsoidal chamber diameter. It thus reproduces the same mantle fraction associated with the analogous flowfield that arises in a hemispherical vortex chamber with a predominantly Beltramian motion.

I. Introduction

THEORETICAL descriptions of wall-bounded cyclonic flowfields have continued to attract sustained interest within the fluid dynamics and propulsion communities, and this may be attributed to their direct relevance to swirl-augmented combustion systems and advanced thrust chamber concepts presently under development. Representative applications include, among others, the Vortex Injection Hybrid Rocket Engine (VIHRE) conceived by Knuth et al. [1, 2], the Vortex Combustion Combined Cycle (VCCC) engine introduced by Chiaverini et al. [3], the Vortex Combustion Cold-Wall (VCCW) engine developed by Chiaverini et al. [4], as well as the VR35K-A VORTEX® engine presently under development by Sierra Space Corporation. A defining characteristic shared by these configurations is the emergence of a bidirectional, coaxial flow structure comprising an inner, nozzle-directed core vortex and an outer, headwall-directed annular vortex. These two regions are separated by an axially rotating yet radially stationary interfacial layer commonly referred to as the 'mantle.'

To date, the majority of analytical and numerical investigations of cyclonic motions have been restricted to cylindrical or conical chamber geometries, although a few studies have considered hemispherical configurations [5–7]. Such geometries pertain to both propulsion devices and industrial cyclone separators employed in particulate filtration systems. From a computational standpoint, most studies have relied on Reynolds-averaged Navier–Stokes (RANS) formulations, although selected efforts have also explored large eddy simulations (LES), finite-element, and finite-difference approaches. In this context, one may cite the investigations of Hsieh and Rajamani [8], Ogawa [9], Hoekstra et al. [10, 11], Derksen and van den Akker [12], Fang et al. [13], Hu et al. [2], Cortes and Gil [14], Zhu et al. [15], Molina et al. [16], Majdalani and Chiaverini [17], and Sharma et al. [18–20], among others.

In complementing these numerical efforts, a number of analytical formulations have been advanced, and some of these trace their origins to the pioneering treatment of conical cyclones by Bloor and Ingham [21]. This line of inquiry is subsequently extended through the development of Beltramian and generalized Beltramian solutions for conical domains by Barber and Majdalani [22] and Majdalani [23], respectively. With respect to the scaling considerations necessary to capture cyclonic-flow instabilities, reference may be made to the analyses of Grimble and Agarwal [24] and Grimble et al. [25]. While analytical solutions in confined conical geometries remain comparatively sparse, a growing body of work exists for cylindrical chambers. These solutions are commonly classified into inviscid, viscous, and compressible formulations. For example, Vyas and Majdalani [26] derive an exact Euler solution by prescribing a

*Graduate Research Assistant, Department of Aerospace Engineering, AIAA University Student Member 1799648.
†Professor and Francis Chair, Department of Aerospace Engineering, AIAA Lifetime Fellow 199546.

linear dependence between the azimuthal vorticity and the streamfunction. Their vorticity-stream function approach is further generalized to produce Beltramian and Trkalian families of solutions through appropriate modifications of the stagnation enthalpy and specific angular momentum relations [27]. Along similar lines, using the Bragg–Hawthorne equation as a starting point, Cecil and Majdalani [28] have extended the generalized Beltramian class to right-cylindrical cyclonic chambers comprising hollow cores.

Another aspect of the theoretical development of cyclonic solutions relates to the systematic incorporation of viscous effects within cylindrical configurations. By building upon the foundational analyses of Mayer and Stowe [29], Maicke and Majdalani [30] manage to examine two alternative representations for the swirl velocity: a Rankine-type piecewise model and a matched-asymptotic formulation that reconciles the inviscid outer field with the forced viscous core. The latter approach permits a smooth transition between the far-field solution and the viscous core region [31, 32]. Along similar lines, Majdalani and Chiaverini [33] apply matched-asymptotic expansions to incorporate viscous corrections into the inviscid solution of Vyas and Majdalani [26], thereby enforcing the requisite no-slip and regularity conditions at both the cylindrical wall and chamber axis, respectively.

Given that many practical realizations of cyclonic motion operate at appreciable flow speeds, the inclusion of compressibility effects has also received attention. In this context, Maicke et al. [34] pursue a compressibility correction to the inviscid Trkalian class of solutions using a multidimensional Rayleigh–Janzen (RJ) expansion, namely, one that incorporates the leading-order dilatational effects in wall-bounded cylindrical chambers. A similar high-speed flow expansion of a Beltramian field in a hemispherically-bounded cyclonic chamber is carried out by Little and Majdalani [35]. Therein, a composite group parameter that combines the injection Mach number and Ekman-type inflow parameter is identified to effectively scale all compressibility-induced distortions of the mantle interface and vortex core surface.

Naturally, in moving past cylindrical and conical formulations, several investigations have begun exploring the topology of cyclonic motions in spherically-bounded domains. A natural starting point is Hill's vortex [36], which describes a spherical region of uniform vorticity translating steadily through an otherwise irrotational fluid under the action of its self-induced velocity. Using an RJ expansion, Moore and Pullin [37] obtain this vortex motion's compressible counterpart asymptotically and, using a global spectral approach, Protas and Elcrat [38] extend the earlier work of Moffatt and Stewartson [39] by characterizing the intrinsic instability of Hill's vortex to axisymmetric perturbations. Exact solutions for steadily propagating swirling spherical vortices in a rotating ideal fluid are later derived by Scase and Terry [40] and, in a related study, Crowe et al. [41] employ numerical simulations and asymptotic expansions in the inverse Rossby number to quantify the decay of the vortex translation speed and radius in weakly rotating environments. In similar vein, Viúdez [42] confirms the role of Hill's vortex as the swirl-free limit of the Hicks–Moffatt dipole, identifying it as the fundamental member of a multipolar family of spherical solutions to the steady vorticity equation.

In addition to these external spherical configurations, and motivated in large part by vortex engine concepts under development at Sierra Space Corporation, several incompressible models have been developed for confined hemispherical chambers. Some of these efforts have culminated in exact irrotational [5], quasi complex-lamellar [6], and inviscid Beltramian solutions for hemispherically-bounded cyclonic flows [7]. Related work by Little [43] has further explored and generalized these analytical formulations in spherical and hemispherical enclosures. However, the semi-ellipsoidal chamber configuration, which has been proposed in connection with next-generation vortex engine concepts, has yet to be addressed. Schematics of such a chamber are furnished in Figs. 1a and 1b.

Despite the abundance of numerical and experimental studies devoted to confined cyclonic motions [18, 44, 45], analytical models capable of accurately describing vortex dynamics within semi-ellipsoidal enclosures remain conspicuously absent. Although prior investigations have demonstrated that right-cylindrical chambers exhibit well-defined pressure and velocity distributions, the geometric curvature inherent to ellipsoidal configurations introduces fundamentally new features that merit independent examination. Accordingly, the present work extends existing formulations of cyclonic motion by accounting explicitly for the curvature effects imposed by a semi-ellipsoidal boundary. The resulting incompressible and inviscid Beltramian solution is intended to serve as a foundational benchmark for subsequent analytical, computational, and experimental studies. It is further anticipated that this framework will facilitate future extensions that take into account dilatational effects and matched-asymptotic corrections that capture both wall and core boundary layers.

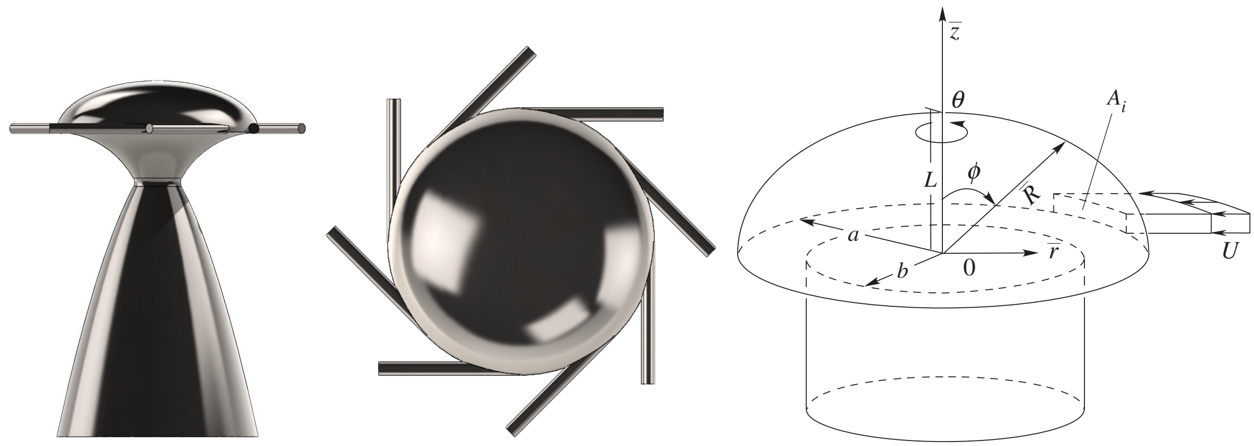

a) Side view **b)** Top view **c)** Geometric model

Fig. 1. Semi-ellipsoidal chamber depicting both a) side and b) top views along with c) the idealized geometric model adopted in the present Beltramian formulation of the cyclonic flowfield.

II. Problem Formulation

We consider the cyclonic, bidirectional motion inside a semi-ellipsoidal chamber that is capped by an equatorial base plane. In this spheroidal domain of equatorial radius a, and polar semi-axis L, which is shown in Fig. 1c, we let $(\bar{r}, \theta, \bar{z})$ and $(\overline{R}, \phi, \theta)$ denote the cylindrical and spherical coordinates with an axis of symmetry $\bar{z}$, and a polar angle ϕ, which is measured from the $+\bar{z}$ zenith. We also allow for an outlet radius b in the base plane at $\bar{z} = 0$. Using overbars to denote dimensional variables, we have

$$\bar{r} = \overline{R}\sin\phi, \qquad \bar{z} = \overline{R}\cos\phi, \qquad \overline{R} = \sqrt{\bar{r}^2 + \bar{z}^2}, \qquad \bar{r} \in [0, a], \qquad \bar{z} \in [0, L], \qquad \phi \in [0, \pi/2]. \tag{1}$$

As such, the domain of interest remains bounded by $\bar{r}^2/a^2 + \bar{z}^2/L^2 = 1$.

A. Basic Assumptions and Governing Equation

As a first approximation, the flow may be taken to be steady, inviscid, incompressible, homogeneous, single-phase, non-reactive, and axisymmetric. These conditions give rise to an isentropic motion. Furthermore, the source of the incoming stream may be reasonably taken to be the same common fluid reservoir that is maintained at a uniform stagnation temperature. Using $\hat{u}$ to denote the specific internal energy, it may be readily seen that the resulting homenergic or homenthalpic flowfield will exhibit the same stagnation enthalpy, $\hat{H} = \hat{u} + \overline{p}/\rho + \bar{\boldsymbol{u}} \cdot \bar{\boldsymbol{u}}/2$, on all of its streamlines. It follows that, by dismissing the effects of gravity or potential energy due to spatial variations within the chamber, the stagnation pressure head, $\overline{H} = \overline{p}/\rho + \bar{\boldsymbol{u}} \cdot \bar{\boldsymbol{u}}/2$, becomes closely related to the stagnation enthalpy through $\overline{H} = \hat{H} - \hat{u}$. Then, using $\hat{s}$ for the specific entropy and $\overline{T}$ for the temperature, the Crocco–Vázsonyi equation returns $\overline{\nabla}\hat{H} = \bar{\boldsymbol{u}} \times \bar{\boldsymbol{\omega}} + \overline{T}\overline{\nabla}\hat{s}$; for an isentropic motion, this reduces to $\overline{\nabla}\overline{H} + \overline{\nabla}\hat{u} = \bar{\boldsymbol{u}} \times \bar{\boldsymbol{\omega}}$. As such, the flow becomes homentropic everywhere, with $\overline{\nabla}\hat{s} = 0$ across all streamlines so long as the Lamb acceleration vector, $\bar{\boldsymbol{\omega}} \times \bar{\boldsymbol{u}}$, remains vanishingly small. Not only will this condition hold for an irrotational motion, it also stands for any rotational motion exhibiting parallel velocity and vorticity vectors, particularly, the class of Beltramian helical fields that we seek to derive. Moreover, the invariance of the stagnation head along streamlines enables us to write, $\overline{H}(\psi) = \overline{p}/\rho + |\bar{\boldsymbol{u}}|^2/2$.

B. Normalization

To facilitate the attendant analysis, it is convenient to introduce a set of dimensionless variables. Following Vyas and Majdalani [26], we define the modified swirl number as $\sigma \equiv a^2/A_i$. This parameter enables us to model the addition of identical injectors by simply accounting for the increase in the total inlet area, A_i. We also introduce the geometric aspect ratio, $l \equiv L/a$, and the normalized exit radius, $\beta \equiv b/a$. Using overbars to denote dimensional quantities, the main non-dimensional variables can be written as

$$\begin{cases} r = \dfrac{\bar{r}}{a}, \;\; R = \dfrac{\overline{R}}{a}, \;\; z = \dfrac{\bar{z}}{a}, \;\; \kappa = \dfrac{1}{2\pi\sigma l}, \;\; \psi = \dfrac{\overline{\psi}}{Ua^2}, \;\; H = \dfrac{\overline{H}}{U^2}, \;\; B = \dfrac{\overline{B}}{aU}, \\ u_r = \dfrac{\bar{u}_r}{U}, \;\; u_\theta = \dfrac{\bar{u}_\theta}{U}, \;\; u_z = \dfrac{\bar{u}_z}{U}, \;\; u_R = \dfrac{\bar{u}_R}{U}, \;\; u_\phi = \dfrac{\bar{u}_\phi}{U}, \;\; p = \dfrac{\bar{p}}{\rho U^2}, \;\; \text{and } \nabla = \overline{\nabla} a. \end{cases} \tag{2}$$

where κ serves as the dimensionless inflow parameter. In cylindrical coordinates, the semi-ellipsoidal domain becomes bounded by $r^2 + z^2/l^2 = 1$, $z \geq 0$, or in spherical coordinates:

$$0 \leq R \leq R_0(\phi); \qquad R_0(\phi) \equiv \frac{l}{\sqrt{\cos^2\phi + l^2 \sin^2\phi}}. \tag{3}$$

Naturally, the special case of $l = 1$ returns $R_0(\phi) \equiv 1$, i.e., a hemisphere of unit radius.

C. Streamfunction and Swirl Function

The velocity components may be expressed in term of the Stokes streamfunction ψ in both cylindrical and spherical coordinates using

$$u_r = -\frac{1}{r}\frac{\partial\psi}{\partial z}, \qquad u_z = \frac{1}{r}\frac{\partial\psi}{\partial r}, \qquad u_R = \frac{1}{R^2\sin\phi}\frac{\partial\psi}{\partial\phi}, \qquad \text{and} \qquad u_\phi = -\frac{1}{R\sin\phi}\frac{\partial\psi}{\partial R}. \tag{4}$$

As for the azimuthal or tangential velocity, it may be expressed in terms of the specific angular-momentum function $B(\psi) \equiv r\,u_\theta$, namely,

$$u_\theta = \frac{B(\psi)}{r} = \frac{B(\psi)}{R\sin\phi}. \tag{5}$$

D. Homogeneous Bragg–Hawthorne Equation for a Swirling Beltramian Motion

For steady, axisymmetric, and inviscid swirling motion, ψ must satisfy Euler's equation or, equivalently, the Bragg–Hawthorne equation, which is given by

$$\frac{\partial^2\psi}{\partial R^2} + \frac{\sin\phi}{R^2}\frac{\partial}{\partial\phi}\left(\frac{1}{\sin\phi}\frac{\partial\psi}{\partial\phi}\right) = R^2\sin^2\phi\,\frac{\mathrm{d}H}{\mathrm{d}\psi} - B(\psi)\frac{\mathrm{d}B}{\mathrm{d}\psi}. \tag{6}$$

Forthwith, the physical constraints associated with a cyclonic Beltramian model consist of:

1. Uniform stagnation head across streamlines: $H(\psi) \equiv H_0$ or $\mathrm{d}H/\mathrm{d}\psi = 0$.

2. Linear Beltramian swirl closure for constant $C > 0$: $B(\psi)\mathrm{d}B/\mathrm{d}\psi = C^2\psi$ or $B(\psi) = \sqrt{B_0^2 + C^2\psi^2}$,

where B_0 denotes an integration constant that can be prescribed by a reference swirl condition in the base plane. As for C, it denotes a constant Beltramian wavenumber that will be later determined from the impermeable wall condition. In view of these conditions, Eq. (6) reduces to a homogeneous Helmholtz equation of the form

$$\frac{\partial^2\psi}{\partial R^2} - \frac{\cot\phi}{R^2}\frac{\partial\psi}{\partial\phi} + \frac{1}{R^2}\frac{\partial^2\psi}{\partial\phi^2} + C^2\psi = 0. \tag{7}$$

As for the boundary conditions, they must account for the presence of an impermeable wall, a bounded velocity at the centerline, mass conservation in the base plane, and a prescribed tangential velocity at entry. Mathematically, these requirements translate into:

(i) The no-through-flow at the wall turns the wall into a streamline that can be specified by $\psi\big|_{r^2+z^2/l^2=1} = \psi_0 =$ constant. With no loss of generality, one can set $\psi_0 = 0$ such that $\psi\big|_{r^2+z^2/l^2=1} = 0$ and $\psi\big(R_0(\phi), \phi\big) = 0$.

(ii) A regular velocity that remains bounded at $r = 0$ requires setting $\psi(r = 0, z) = 0$.

(iii) Mass conservation in the base plane requires an inflow-outflow balance at $z = 0$ that remains consistent with

$$\int_0^\beta u_z(r, 0)\, r\, \mathrm{d}r = \kappa\, l, \tag{8}$$

where β denotes the mantle outlet radius. Using $u_z r = \psi_r$, Eq. (8) becomes $\psi(\beta, 0) - \psi(0, 0) = \kappa l$ or $\psi(\beta, 0) = \kappa l$, since $\psi(0, 0) = 0$.

(iv) For a prescribed tangential velocity at entry in the base plane, one has $\bar{u}_\theta = U$; as such, one can set $u_\theta(1, 0) = B(1, 0) = 1$ and deduce $B_0 = 1$.

III. Exact Beltramian Solution

For general $l \neq 1$, Eq. (3) is not a spherical coordinate surface $R = \text{const}$, so spherical separation cannot be enforced directly. Instead, one may use spheroidal coordinates where the wall is a coordinate surface.

In what follows, we present the oblate case ($0 < l < 1$) realizing that the prolate case ($l > 1$) remains analogous. For $l \neq 1$, the semi-ellipsoidal wall is not a surface of constant spherical radius R. As such, the Beltramian Helmholtz equation cannot be separated exactly in spherical coordinates. As a remedy, we introduce spheroidal coordinates in which the ellipsoidal boundary coincides with a coordinate surface. This procedure leads to a fully separable formulation of Eq. (7) that yields an exact eigenvalue problem for the Beltramian Type 1 flow in a semi-ellipsoidal chamber.

A. Oblate Spheroidal Coordinates (Oblate Semi-Ellipsoid, $0 < l < 1$)

To start, we define the focal length and coordinate constant using

$$f = \sqrt{1 - l^2}, \qquad \xi_0 = \frac{l}{\sqrt{1 - l^2}} = \frac{l}{f}. \tag{9}$$

The corresponding spheroidal coordinates, (ξ, η, θ), can be expressed as

$$r = f\sqrt{(1 + \xi^2)(1 - \eta^2)} \qquad \text{and} \qquad z = f\xi\eta; \qquad 0 \leq \xi \leq \xi_0,\ 0 \leq \eta \leq 1. \tag{10}$$

In this notation, the wall surface given by $r^2 + z^2/l^2 = 1$ turns into $\xi = \xi_0$. Furthermore, one may introduce the spheroidal parameter as

$$\gamma \equiv Cf = C\sqrt{1 - l^2}. \tag{11}$$

B. Separation and Oblate Spheroidal ODEs

By seeking separable solutions of the form

$$\psi(\xi, \eta) = A\, R_1(\gamma, \xi)\, S_1(\gamma, \eta), \tag{12}$$

we arrive at the oblate spheroidal wave equations

$$\frac{d}{d\eta}\left[(1 - \eta^2)\frac{\mathrm{d}S_1}{d\eta}\right] + \left(\lambda - \gamma^2\eta^2 - \frac{1}{1 - \eta^2}\right)S_1 = 0, \tag{13}$$

$$\frac{d}{d\xi}\left[(1 + \xi^2)\frac{\mathrm{d}R_1}{d\xi}\right] + \left(\lambda + \gamma^2\xi^2 - \frac{1}{1 + \xi^2}\right)R_1 = 0, \tag{14}$$

where $\lambda = \lambda(\gamma)$ denotes the separation constant. This constant $\lambda = \lambda_n(\gamma)$ arises from a discrete eigenvalue problem, where the integer $n = \{1, 2, \ldots\}$ denotes the radial (or polar) mode number. In the present work, attention is restricted to the fundamental polar-radial mode of $n = 1$, which yields the simplest Beltramian motion and recovers the hemispherical Type-1 solution in the spherical limit. As for the angular dependence, it corresponds to the azimuthal order m of the spheroidal wave family. For an axisymmetric Stokes streamfunction formulation, regularity at the axis enforces $m = 1$, hence giving rise to the separated spheroidal functions R_1 and S_1. In practice, $R_1(\gamma, \xi)$, $S_1(\gamma, \eta)$, and the coupled separation constant $\lambda(\gamma)$ can be evaluated numerically using standard spheroidal wave routines (e.g. `SpheroidalPS` and `SpheroidalQS` in Mathematica), with admissible values of γ being retrievable from the wall eigencondition $R_1(\gamma, \xi_0) = 0$.

C. Eigenproblem and Wall Boundary Condition

The wall condition $\psi(\xi_0, \eta) = 0$ reduces to the eigenvalue constraint

$$R_1(\gamma, \xi_0) = 0, \tag{15}$$

which determines the admissible Beltramian wavenumber, $\gamma = C\sqrt{1 - l^2}$.

D. Normalization Constant

The amplitude A is fixed by the base-plane condition $\psi(\beta, 0) = \kappa l$. At $z = 0$ we have $\eta = 0$ and $r = f\sqrt{1 + \xi^2}$. As such, the outlet radius $r = \beta$ corresponds to $\xi_\beta = \sqrt{(\beta/f)^2 - 1}$ with $\beta \geq f$. Then by setting $\psi(\beta, 0) = \kappa l$, we get

$$A = \frac{\kappa l}{R_1(\gamma, \xi_\beta)\, S_1(\gamma, 0)}. \tag{16}$$

E. Recovery of the Hemispherical Solution

The hemispherical chamber may be readily recovered as a limiting case when the geometric aspect ratio approaches unity, i.e. $l \to 1$. In this limit, both the focal length, $f = \sqrt{1 - l^2}$, and the spheroidal Beltramian parameter, $\gamma = Cf$, vanish identically, regardless of the value of the Beltramian wavenumber, C.

As $\gamma \to 0$, the oblate spheroidal coordinates degenerate smoothly into spherical coordinates, with $\eta = \cos\phi$ and $\xi \sim R/f$. In this limit, the spheroidal angular equation given by Eq. (13) reduces to the Legendre equation with $\lambda \to 2$. Moreover, the regular $m = n = 1$ solution becomes

$$S_1(\gamma, \eta) \sim 1 - \eta^2 = \sin^2\phi. \tag{17}$$

Similarly, the radial spheroidal equation given by Eq. (14) reduces to the spherical Riccati–Bessel equation for the $n = 1$ Beltramian mode. The corresponding bounded solution assumes the form

$$R_1(\gamma, \xi) \sim \frac{CR\cos(CR) - \sin(CR)}{R}, \tag{18}$$

where $R = \sqrt{r^2 + z^2}$ returns the spherical radius. Accordingly, the streamfunction becomes

$$\psi(R, \phi) \sim \sin^2\phi\, \frac{CR\cos(CR) - \sin(CR)}{R}, \tag{19}$$

which is precisely the Type 1 Beltramian solution previously obtained for a hemispherical chamber [7]. This confirms that the present spheroidal formulation constitutes an exact generalization of the hemispherical Beltramian vortex to semi-ellipsoidal geometries. In what follows, all velocity expressions correspond to the fundamental Beltramian eigenmode characterized by $(m, n) = (1, 1)$.

F. Velocity Components for the $n = 1$ Semi-Ellipsoidal Beltramian Solution

1. Cylindrical Velocities

Given $\psi(\xi, \eta)$, the cylindrical components may be retrieved from Eqs. (4) and (5). For the $n = 1$ Beltramian mode, we can put

$$\psi_\xi = A\, R_1'(\gamma, \xi)\, S_1(\gamma, \eta),\ \psi_\eta = A\, R_1(\gamma, \xi)\, S_1'(\gamma, \eta),\ Q = \xi^2 + \eta^2,\ z = f\xi\eta,\ \text{and } r = f\sqrt{(1 + \xi^2)(1 - \eta^2)}. \tag{20}$$

The cylindrical meridional velocities in terms of (ξ, η) and spheroidal derivatives can be expressed as

$$u_r(\xi, \eta) = \frac{A}{f\, r\, Q}\Big[\xi(1 - \eta^2)\, R_1(\gamma, \xi)\, S_1'(\gamma, \eta) \ + \ \eta(1 + \xi^2)\, R_1'(\gamma, \xi)\, S_1(\gamma, \eta)\Big], \tag{21}$$

$$u_z(\xi, \eta) = \frac{A}{f^2 Q}\Big[\eta\, R_1(\gamma, \xi)\, S_1'(\gamma, \eta) \ - \ \xi\, R_1'(\gamma, \xi)\, S_1(\gamma, \eta)\Big]. \tag{22}$$

The swirl velocity follows from Eq. (5), namely,

$$u_\theta(\xi,\eta) = \frac{1}{r(\xi,\eta)}\sqrt{B_0^2 + C^2\psi(\xi,\eta)^2} = \frac{1}{r(\xi,\eta)}\sqrt{1 + C^2A^2R_1(\gamma,\xi)^2S_1(\gamma,\eta)^2}. \tag{23}$$

Because the semi-ellipsoidal boundary is represented exactly in oblate spheroidal coordinates, it is most convenient to evaluate the meridional velocities directly in (ξ,η), and then map them into cylindrical space using $r = f\sqrt{(1+\xi^2)(1-\eta^2)}$ and $z = f\xi\eta$. In practice, Eqs. (21) and (22) constitute the primary implementation-ready expressions for (u_r, u_z), while the swirl velocity follows immediately from the Beltramian swirl function, $u_\theta = B(\psi)/r$.

2. Spherical Velocities

If ψ is expressed directly as $\psi(R,\phi)$, one can use Eqs. (4) and (5) to obtain

$$u_R(R,\phi) = \frac{1}{R^2\sin\phi}\frac{\partial\psi}{\partial\phi}, \qquad u_\phi(R,\phi) = -\frac{1}{R\sin\phi}\frac{\partial\psi}{\partial R}, \qquad \text{and} \qquad u_\theta(R,\phi) = \frac{\sqrt{1 + C^2\psi(R,\phi)^2}}{R\sin\phi}. \tag{24}$$

If ψ is computed in spheroidal form and velocities are available in cylindrical form, one may use

$$u_R = u_r\sin\phi + u_z\cos\phi, \qquad u_\phi = u_r\cos\phi - u_z\sin\phi, \qquad \text{and} \qquad u_\theta = u_\theta, \tag{25}$$

with $\sin\phi = r/R$ and $\cos\phi = z/R$. By substituting the geometric definitions of r and z from Eq. (20), the trigonometric terms become purely a function of (ξ,η), namely,

$$\sin\phi = \frac{\sqrt{(1+\xi^2)(1-\eta^2)}}{\sqrt{1+\xi^2-\eta^2}} \quad \text{and} \quad \cos\phi = \frac{\xi\eta}{\sqrt{1+\xi^2-\eta^2}}. \tag{26}$$

Inserting these relations alongside the cylindrical meridional velocities from Eq. (21) and Eq. (22) into Eq. (25) allows for substantial algebraic reduction. The resulting spherical velocities can be elegantly expressed in the oblate spheroidal domain as

$$u_R(\xi,\eta) = \frac{A}{fRQ}\left[\xi R_1(\gamma,\xi)S_1'(\gamma,\eta) + \eta R_1'(\gamma,\xi)S_1(\gamma,\eta)\right], \tag{27}$$

$$u_\phi(\xi,\eta) = \frac{A}{RQr}\left[\eta(1-\eta^2)R_1(\gamma,\xi)S_1'(\gamma,\eta) - \xi(1+\xi^2)R_1'(\gamma,\xi)S_1(\gamma,\eta)\right]. \tag{28}$$

Note that the geometric parameters R, Q, and r are retained in the denominators to maintain compactness. The swirl velocity remains identical to Eq. (23) due to the shared azimuthal coordinate.

G. Streamlines and Mantle Distribution

For visualization purposes, vector streamline plots derived mainly from Eqs. (21) and (22) are shown in Fig. 2. This is accomplished by setting $l = 0.4, 0.6$, and 0.8, all of which correspond to an oblate semi-ellipsoidal configuration. The exact $n = 1$ Beltramian solution is also displayed alongside its complex-lamellar counterpart for these three aspect ratios to facilitate direct comparisons. As established previously, an aspect ratio of $l = 1$ seamlessly recovers the hemispherical solution extensively studied by Williams and Majdalani [7]. To better delineate the internal flow boundaries, the axial ($u_z = 0$) and polar ($u_\phi = 0$) mantles are evaluated numerically and superimposed using broken and chained lines, respectively. At the time of this writing, the exact mathematical expressions for these mantles remain strictly implicit due to the highly transcendental nature of the underlying spheroidal wave functions.

At first glance, both models successfully capture the signature bidirectional and helical motion characteristic of cyclonic rocket engines: the injected fluid ascends along the curved semi-ellipsoidal wall, turns inward near the headend, reverses its axial direction, and exits through a centrally located inner flow region. However, a closer inspection reveals distinct behavioral differences in how the two solutions partition this domain. In the Beltramian formulation, the flow reversal occurs appreciably closer to the centerline compared to the complex-lamellar case. It therefore produces a tighter descending inner core. This localized flow restriction is likely driven by the smaller chamber exit radius, β, that is inherently accommodated by the Beltramian boundary conditions.

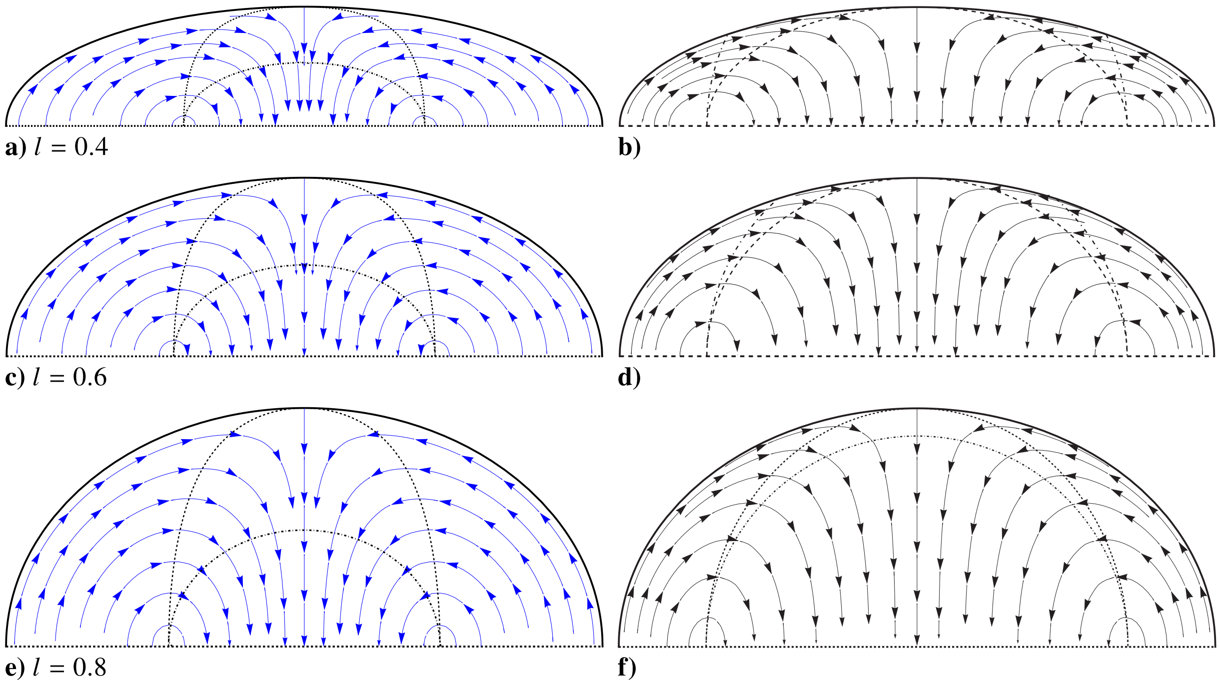

Fig. 2. Vector streamlines of a semi-ellipsoidal oblate chamber taken in the r-z plane and showing a, c, e) Beltramian (left side) and b, d, f) complex-lamellar solutions (right side) for aspect ratios of $l = 0.4, 0.6,$ and 0.8. The loci of axial mantles ($u_z = 0$; – – –) as well as polar mantles ($u_\phi = 0$; — · —) are displayed using $\kappa = 0.05$.

Furthermore, the geometric relation between the two mantles brings into perspective a fundamental departure from the complex-lamellar model. In the complex-lamellar solution, the mantles are known to merge completely at a critical aspect ratio of $l = 1/\sqrt{2}$ (≈ 0.707). In stark contrast, the Beltramian mantles exhibit no such convergence; they remain strictly distinct and clearly separated across all evaluated aspect ratios. As illustrated in Fig. 2, not only do the mantles resist merging, but the spatial gap between them expands dramatically as the chamber aspect ratio is increased. For highly oblate configurations, such as $l = 0.4$, the polar and axial mantles remain tightly nested. However, as l increases to 0.6 and 0.8, the broken lines demarcating the axial mantle expand significantly outward, actively encapsulating the chained polar mantle lines and vastly increasing the volume of the intermediate fluid zone between the two boundaries.

This distinct separation fundamentally dictates the chamber's volumetric utilization. While the axial mantle equally bisects the domain into an upward-flowing outer annulus and a downward-flowing inner core, the polar mantle extends deeper toward the centerline, thus forming a much more compact inner region. Clearly, the polar mantle surface remains physically smaller while sitting at a lower centroidal elevation than its axial counterpart. From a propulsion design perspective, this reduced interfacial crossflow area restricts premature inward fluid migration. In a practical cyclonic combustor, this advantageously mitigates the early leakage of freshly injected oxidizer streams into the exhaust core, thereby promoting superior mixing and combustion efficiency within the upper dome.

It is, perhaps, equally important to examine the effect of the swirl parameter κ on the fluid motion, given that it serves as the formulation's sole similarity parameter. While every velocity component scales proportionally with κ, this parameter does not inherently alter the meridional kinematics within the r-z plane. Because these streamlines remain independent of the swirl intensity, our analysis naturally pivots to evaluating how κ governs the overall flow dynamics within the r-θ plane.

To properly assess this behavior, a representative horizontal cross-section must be established at an appropriate centroidal elevation. Accounting for the geometry's aspect ratio, this optimal plane is universally defined at a height of $z = (3/8)l$. Evaluating the flowfield at this specific elevation provides an ideal vantage point to quantify the relative contributions of the radial and azimuthal velocity components, yielding a ratio of $|u_r/u_\theta| = |\partial\psi/\partial z|\left(1 + C^2\psi^2\right)^{-1/2}$.

By expanding upon the baseline value of $\kappa = 0.05$ used in Fig. 2, Fig. 3 illustrates the flow's behavior for representative swirl parameters of $\kappa = 0.01$ and 0.1. As κ increases from 0.01 to 0.1, the swirling nature of the flow visibly attenuates. While theoretically larger values (such as $\kappa \geq 1$) would cause the radial velocity component to

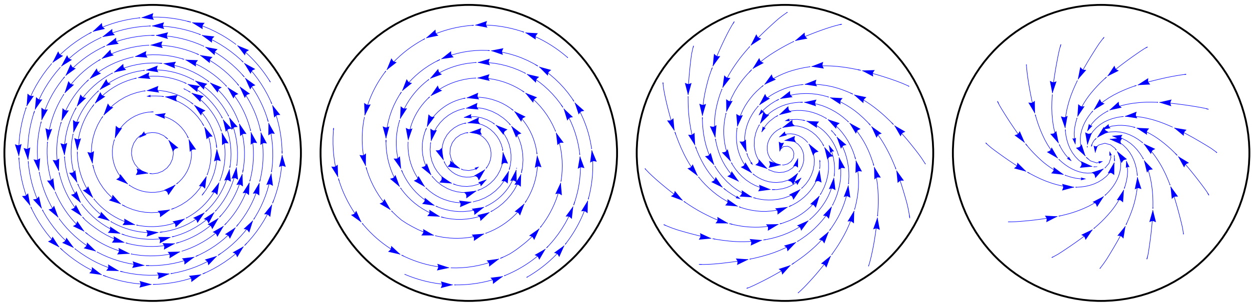

a) $\kappa = 0.01$ **b)** 0.1 **c)** $z = 0.25$ **d)** 0.5

Fig. 3. Top-view streamline topologies in an oblate chamber ($l = 0.8$). From left to right, subfigures (a) and (b) illustrate the flowfield evaluated at a constant centroidal elevation of $z = (3/8)l$ for inflow parameters of $\kappa = 0.01$ and 0.1, respectively. Subfigures (c) and (d) illustrate the shrinking active cross-section for a constant inflow parameter of $\kappa = 1$ at ascending elevations of $z = 0.25$ and 0.5, respectively.

surpass its azimuthal counterpart and create a minimally spiraling sink flow, the strongly swirling regime remains the primary focus here. In stark contrast, further reductions in κ compel the flow into a highly rotation-dominated state where the inward radial draw is effectively eclipsed by the azimuthal velocity. Under these conditions, the trajectories tighten substantially, collapsing the spirals into tightly-wound, nearly concentric orbits. Consequently, dropping the parameter further down from 0.01 yields no meaningful change to the streamline topology in the r-θ plane.

To thoroughly characterize the three-dimensional kinematics, the analysis must transition from parametric variations of κ to the spatial evolution of the flowfield along the longitudinal axis. By anchoring the swirl parameter at unity ($\kappa = 1$), the streamlines can be tracked across ascending horizontal planes, specifically focusing on elevations of $z = 0.25$ and 0.5 at $l = 0.8$. An examination of these planar slices yields two critical insights into the flow's internal structure. First, regardless of the vertical station, the radial velocity component strictly decays to zero as the radial coordinate approaches the centerline ($r \to 0$). Second, in strict adherence to the chamber's morphological constraints, the outer envelope of the flowfield undergoes continuous radial compression, tapering inward as dictated by the semi-ellipsoidal wall geometry.

IV. Conclusion

In this study, an exact analytical solution is derived for the inviscid, incompressible Beltramian motion of a bidirectional vortex inside a capped semi-ellipsoidal chamber. By employing the Bragg-Hawthorne equation and mapping the domain into oblate spheroidal coordinates, a fully separable formulation is achieved for the Stokes streamfunction. This approach leverages transcendental spheroidal wave functions to rigorously satisfy the impermeable wall condition and, in the process, yield exact analytical expressions for the spatial velocities in both cylindrical and spherical coordinate systems. It is gratifying that this parent formulation seamlessly recovers the previously established hemispherical solution as the geometric aspect ratio approaches unity [7].

Overall, the Beltramian flowfield successfully captures the signature bidirectional and helical characteristics of practical cyclonic rocket engines. A comparative analysis shows that the Beltramian flow reversal occurs closer to the centerline than in its complex-lamellar counterpart, hence resulting in a tighter descending inner core. Furthermore, the internal flow boundaries, which may be delineated by the axial and polar mantles, remain clearly distinct across the oblate geometries considered. Unlike the complex-lamellar model where the mantles are known to merge for a given aspect ratio, the Beltramian axial mantle actively envelops the polar mantle over all aspect ratios explored.

The parametric evaluation of the flow topology in the r-θ plane provides further insight into the kinematic behavior of the vortex. By varying the inflow parameter, κ, one may ascertain that the flow transitions from a highly rotation-dominated state at $\kappa = 0.01$ to an increasing sink-like flow as κ grows further. At low κ values, the trajectories collapse into tightly-wound, nearly concentric orbits, whereas higher κ values ensure that the radial flow contribution becomes the primary driver of the r-θ kinematics.

As we travel from the equatorial plane vertically upward, the spatial evolution of the r-θ flow structures along the longitudinal axis reflects the continuous radial compression of the active vortex envelope. As the horizontal crosssections ascend from the equatorial base toward the geometric apex, the flowfield tapers inward, accurately reflecting the morphological constraints imposed by the semi-ellipsoidal wall geometry. This distinct geometric separation and the resulting spatial tapering fundamentally dictate the chamber's internal volumetric utilization.

From a propulsion design perspective, the reduced interfacial crossflow area associated with the Beltramian mantles restricts premature inward fluid migration. In a practical cyclonic combustor, this advantageously mitigates the early leakage of freshly injected oxidizer streams into the exhaust core, thereby promoting superior mixing and combustion efficiency within the upper dome. Ultimately, this exact Beltramian solution may serve as a foundational theoretical benchmark for modeling semi-ellipsoidal cyclonic combustors. It establishes a rigorous mathematical framework that paves the way for future modeling efforts, including matched-asymptotic corrections to capture viscous boundary layers and the systematic incorporation of compressibility effects.

References

[1] Knuth, W. H., Bemowski, P. A., Gramer, D. J., Majdalani, J., and Rothbauer, W. J., "Gas-Fed, Vortex Injection Hybrid Rocket Engine," SBIR Phase I, NASA Final Technical Contract No. NAS8-40679, Madison, Wisconsin, August 1996.

[2] Knuth, W. H., Chiaverini, M. J., Sauer, J. A., and Gramer, D. J., "Solid-Fuel Regression Rate Behavior of Vortex Hybrid Rocket Engines," *Journal of Propulsion and Power*, Vol. 18, No. 3, May 2002, pp. 600–609. doi:10.2514/2.5974.

[3] Chiaverini, M. J., Sauer, J. A., and Knuth, W. H., "Final Report on Vortex Combustion Combined Cycle Engine – A Phase I SBIR Project," AFRL Contract No. F04611-99-C-0063, OTC-GS082-FR-99-1, Madison, Wisconsin, March 1999.

[4] Chiaverini, M. J., Malecki, M., Sauer, J. A., Knuth, W. H., and Majdalani, J., "Vortex Thrust Chamber Testing and Analysis for O2-H2 Propulsion Applications," *39th AIAA/ASME/SAE/ASEE Joint Propulsion Conference and Exhibit*, AIAA Paper 2003-4473, July 2003. doi:10.2514/6.2003-4473.

[5] Williams, L. L. and Majdalani, J., "An Exact Irrotational Solution for a Hemispherically Bounded Cyclonic Flowfield," *Physics of Fluids*, Vol. 33, No. 6, June 2021, pp. 063608. doi:10.1063/5.0051111.

[6] Majdalani, J. and Williams, L. L., "A Quasi Complex-Lamellar Solution for a Hemispherically Bounded Cyclonic Flowfield," *Physics of Fluids*, Vol. 33, No. 8, August 2021, pp. 083105. doi:10.1063/5.0058647.

[7] Williams, L. L. and Majdalani, J., "Exact Beltramian Solutions for Hemispherically Bounded Cyclonic Flowfields," *Physics of Fluids*, Vol. 33, No. 8, August 2021, pp. 093601. doi:10.1063/5.0063743.

[8] Hsieh, K. T. and Rajamani, R. K., "Mathematical Model of the Hydrocyclone Based on Physics of Fluid Flow," *AIChE Journal*, Vol. 37, No. 5, May 1991, pp. 735–746. doi:10.1002/aic.690370511.

[9] Ogawa, A., *Vortex Flow*, CRC Press, Boca Raton, Fla, 1993.

[10] Hoekstra, A. J., van Vliet, E., Derksen, J. J., and van den Akker, H. E. A., "Vortex Core Precession in a Gas Cyclone," *Fluid Mechanics and Its Applications*. Springer Netherlands, 1998, pp. 289–292. doi:10.1007/978-94-011-5118-4_71.

[11] Hoekstra, A. J., Derksen, J. J., and van den Akker, H. E. A., "An Experimental and Numerical Study of Turbulent Swirling Flow in Gas Cyclones," *Chemical Engineering Science*, Vol. 54, No. 13-14, July 1999, pp. 2055–2065. doi:10.1016/s0009-2509(98)00373-x.

[12] Derksen, J. J. and van den Akker, H. E. A., "Simulation of Vortex Core Precession in a Reverse-Flow Cyclone," *AIChE Journal*, Vol. 46, No. 7, July 2000, pp. 1317–1331. doi:10.1002/aic.690460706.

[13] Knuth, W. H., Gramer, D. J., Chiaverini, M. J., Sauer, J. A., Whitesides, R., and Dill, R., "Preliminary CFD Analysis of the Vortex Hybrid Rocket Chamber and Nozzle Flow Field," *34th AIAA/ASME/SAE/ASEE Joint Propulsion Conference and Exhibit*, AIAA Paper 1998-3351, July 1998. doi:10.2514/6.1998-3351.

[14] Cortes, C. and Gil, A., "Modeling the Gas and Particle Flow Inside Cyclone Separators," *Progress in Energy and Combustion Science*, Vol. 33, No. 5, October 2007, pp. 409–452. doi:10.1016/j.pecs.2007.02.001.

[15] Zhu, Z., Na, Y., and Lu, Q., "Pressure Drop in Cyclone Separator at High Pressure," *Journal of Thermal Science*, Vol. 17, No. 3, September 2008, pp. 275–280. doi:10.1007/s11630-008-0275-7.

[16] Molina, R., Wang, S., Gomez, L. E., Mohan, R. S., Shoham, O., and Kouba, G., "Wet Gas Separation in Gas-Liquid Cylindrical Cyclone Separator," *Journal of Energy Resources Technology*, Vol. 130, No. 4, nov 2008. doi:10.1115/1.3000101.

[17] Majdalani, J. and Chiaverini, M. J., "Characterization of GO2–GH2 Simulations of a Miniature Vortex Combustion Cold-Wall Chamber," *Journal of Propulsion and Power*, Vol. 33, No. 2, March 2017, pp. 387–397. doi:10.2514/1.b36277.

[18] Sharma, G. and Majdalani, J., "Effects of Nozzle Inlet Size and Curvature on the Flow Development in a Bidirectional Vortex Chamber," *Physics of Fluids*, Vol. 33, No. 9, September 2021, pp. 093607. doi:10.1063/5.0066121.

[19] Sharma, G. and Majdalani, J., "Effects of Various Inlet Parameters on the Computed Flow Development in a Bidirectional Vortex Chamber," *Physics of Fluids*, Vol. 34, No. 4, April 2022, pp. 043607. doi:10.1063/5.0089443.

[20] Sharma, G. and Majdalani, J., "Effects of Various Geometric Parameters on the Computed Swirl Numbers and Flow Topology in a Bidirectional Vortex Chamber," *Physics of Fluids*, Vol. 36, No. 1, January 2024. doi:10.1063/5.0190683.

[21] Bloor, M. I. G. and Ingham, D. B., "The Flow in Industrial Cyclones," *Journal of Fluid Mechanics*, Vol. 178, No. 1, May 1987, pp. 507–519. doi:10.1017/s0022112087001344.

[22] Barber, T. A. and Majdalani, J., "On the Beltramian Motion of the Bidirectional Vortex in a Conical Cyclone," *Journal of Fluid Mechanics*, Vol. 828, September 2017, pp. 708–732. doi:10.1017/jfm.2017.494.

[23] Majdalani, J., "On the Generalized Beltramian Motion of the Bidirectional Vortex in a Conical Cyclone," *Physics of Fluids*, Vol. 34, No. 3, March 2022, pp. 036604. doi:10.1063/5.0083740.

[24] Grimble, T. A. and Agarwal, A., "Characterisation of Acoustically Linked Oscillations in Cyclone Separators," *Journal of Fluid Mechanics*, Vol. 780, September 2015, pp. 45–59. doi:10.1017/jfm.2015.441.

[25] Grimble, T. A., Agarwal, A., and Juniper, M. P., "Local Linear Stability Analysis of Cyclone Separators," *Journal of Fluid Mechanics*, Vol. 816, March 2017, pp. 507–538. doi:10.1017/jfm.2017.89.

[26] Vyas, A. B. and Majdalani, J., "Exact Solution of the Bidirectional Vortex," *AIAA Journal*, Vol. 44, No. 10, October 2006, pp. 2208–2216. doi:10.2514/1.14872.

[27] Majdalani, J., "Helical Solutions of the Bidirectional Vortex in a Cylindrical Cyclone: Beltramian and Trkalian Motions," *Fluid Dynamics Research*, Vol. 44, No. 6, October 2012, pp. 065506. doi:10.1088/0169-5983/44/6/065506.

[28] Cecil, O. M. and Majdalani, J., "On the Generalized Beltramian Motion of the Bidirectional Vortex in a Right-Cylindrical Cyclone with a Hollow Core," *Physics of Fluids*, Vol. 34, No. 4, April 2022, pp. 043603. doi:10.1063/5.0087621.

[29] Mayer, E. W. and Powell, K. G., "Similarity Solutions for Viscous Vortex Cores," *Journal of Fluid Mechanics*, Vol. 238, May 1992, pp. 487–507. doi:10.1017/S0022112092001794.

[30] Maicke, B. A. and Majdalani, J., "A Constant Shear Stress Core Flow Model of the Bidirectional Vortex," *Proceedings of the Royal Society A: Mathematical, Physical and Engineering Sciences*, Vol. 465, No. 2103, March 2009, pp. 915–935. doi:10.1098/rspa.2008.0342.

[31] Lewellen, W. S., "A solution for three-dimensional vortex flows with strong circulation," *Journal of Fluid Mechanics*, Vol. 14, No. 03, November 1962, pp. 420. doi:10.1017/s0022112062001330.

[32] Stewartson, K. and Hall, M. G., "The Inner Viscous Solution for the Core of a Leading-Edge Vortex," *Journal of Fluid Mechanics*, Vol. 15, No. 2, February 1963, pp. 306–318. doi:10.1017/S0022112063000264.

[33] Majdalani, J. and Chiaverini, M. J., "On Steady Rotational Cyclonic Flows: The Viscous Bidirectional Vortex," *Physics of Fluids*, Vol. 21, No. 10, October 2009, pp. 103603. doi:10.1063/1.3247186.

[34] Maicke, B. A., Cecil, O. M., and Majdalani, J., "On the Compressible Bidirectional Vortex in a Cyclonically Driven Trkalian Flow Field," *Journal of Fluid Mechanics*, Vol. 823, June 2017, pp. 755–786. doi:10.1017/jfm.2017.310.

[35] Little, D. S. and Majdalani, J., "On the Compressible Beltramian Vortex in a Hemispherically Bounded Cyclonic Flow Field," *Journal of Fluid Mechanics*, Vol. XXX, No. X, 2026, pp. XXX–XXX. doi:10.1017/jfm.2026.11139.

[36] Hill, M. J. M., "On a Spherical Vortex," *Philosophical Transactions of the Royal Society of London, Series A*, Vol. 185, 1894, pp. 213–245.

[37] Moore, D. W. and Pullin, D. I., "On Steady Compressible Flows with Compact Vorticity; The Compressible Hill's Spherical Vortex," *J. Fluid Mech.*, Vol. 374, 1998, pp. 285–303.

[38] Protas, B. and Elcrat, A., "Linear Stability of Hill's Vortex to Axisymmetric Perturbations," *Journal of Fluid Mechanics*, Vol. 799, June 2016, pp. 579–602. doi:10.1017/jfm.2016.387.

[39] Moffatt, H. K. and Moore, D. W., "The Response of Hill's Spherical Vortex to a Small Axisymmetric Disturbance," *Journal of Fluid Mechanics*, Vol. 87, No. 4, August 1978, pp. 749–760. doi:10.1017/S002211207800186X.

[40] Scase, M. M. and Terry, H. L., "Spherical Vortices in Rotating Fluids," *Journal of Fluid Mechanics*, Vol. 846, 2018, pp. R4–12. doi:10.1017/jfm.2018.334.

[41] Crowe, M. N., Kemp, C. J. D., and Johnson, E. R., "The Decay of Hill's Vortex in a Rotating Flow," *Journal of Fluid Mechanics*, Vol. 919, 2021, pp. A6–24. doi:10.1017/jfm.2021.386.

[42] Viúdez, A., "Multipolar Spherical and Cylindrical Vortices," *Journal of Fluid Mechanics*, Vol. 936, February 2022, pp. A13. doi:10.1017/jfm.2022.73.

[43] Little, D. S., *On Viscous and Compressible Cyclonic Motions in Confined Hemispherical Chambers*, Ph.D. Dissertation, Auburn University, Department of Aerospace Engineering, 2025.

[44] Gupta, R., Kaulaskar, M. D., Kumar, V., Sripriya, R., Meikap, B. C., and Chakraborty, S., "Studies on the Understanding Mechanism of Air Core and Vortex Formation in a Hydrocyclone," *Chemical Engineering Journal*, Vol. 144, No. 2, October 2008, pp. 153–166. doi:10.1016/j.cej.2008.01.010.

[45] Neesse, T. and Dueck, J., "Air Core Formation in the Hydrocyclone," *Minerals Engineering*, Vol. 20, No. 4, April 2007, pp. 349–354. doi:10.1016/j.mineng.2007.01.007.